

Supplementary Information

The Deep Roots of Geology: Tectonic History of Australia and its Margins expressed by Mantle Anisotropy

Caroline M. Eakin¹

¹Research School of Earth Sciences, Australian National University, Canberra, Australia

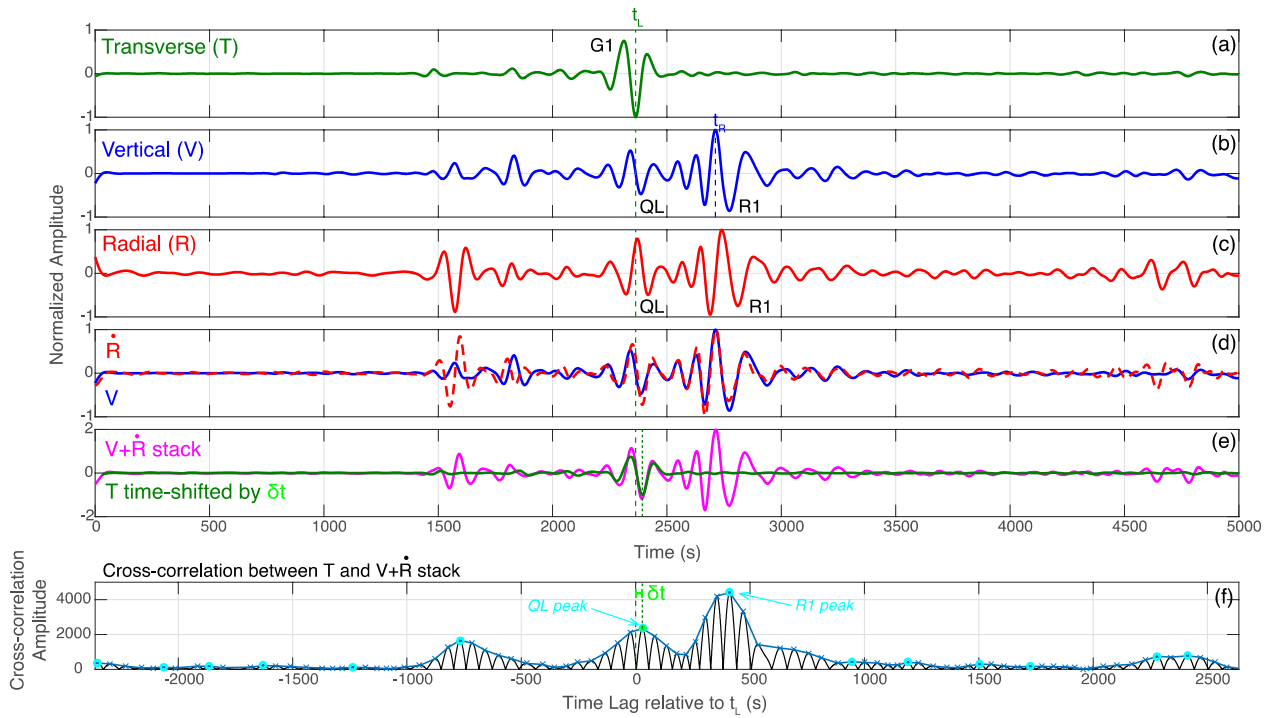


Figure S1. Example of a Quasi-Love (QL) wave measurement from station MORW (see Fig. S2 for location) for a M7.5 event on 19-Aug-2016 in the South Georgia Island Region. The SNR of this event is 16, and the epicentral distance is 92° . All seismograms have been low-pass filtered at 100 seconds. (a-c): A prominent QL wave arrival is visible on both the vertical and radial components that arrives soon after the fundamental Love wave (G1) but before the fundamental Rayleigh wave (R1). The time of peak G1 amplitude is demoted t_L (vertical dashed green line) and peak R1 amplitude t_R (vertical dashed blue line). (d): Similar to R1, the QL wave is 90° out of phase between the vertical and radial components (i.e. elliptical particle motion), as seen here by the good match between the vertical component (blue) and the first-derivative of the radial (dashed red). (e): The vertical component and first-derivative radial component from (d) are stacked (magenta) to emphasize the QL wave. In green, the transverse component is plotted with a time shift of δt , to compare the cross-correlation fit between G1 and QL. (f): Cross-correlation function between the transverse component, and the stacked seismogram from (e) (thin black line), relative to the G1 arrival. The cross-correlation function is periodic (both positive and negative) and thus absolute amplitude is shown. Maxima of the cross-correlation function are marked with small blue crosses to form a new time-series (blue line). Maxima of this new time-series are then marked by cyan circles. The largest amplitude cross-correlation occurs between R1 and G1 (R1 peak). The cross-correlation value between QL and G1 (QL peak; green circle and vertical dotted green line), the parameter of interest, is the first peak after time zero (i.e. first cyan circle) and before the R1 peak. The time-lag of the QL peak, labelled δt , is used in equation 3 to determine the distance to the scatterer (see Fig. S2).

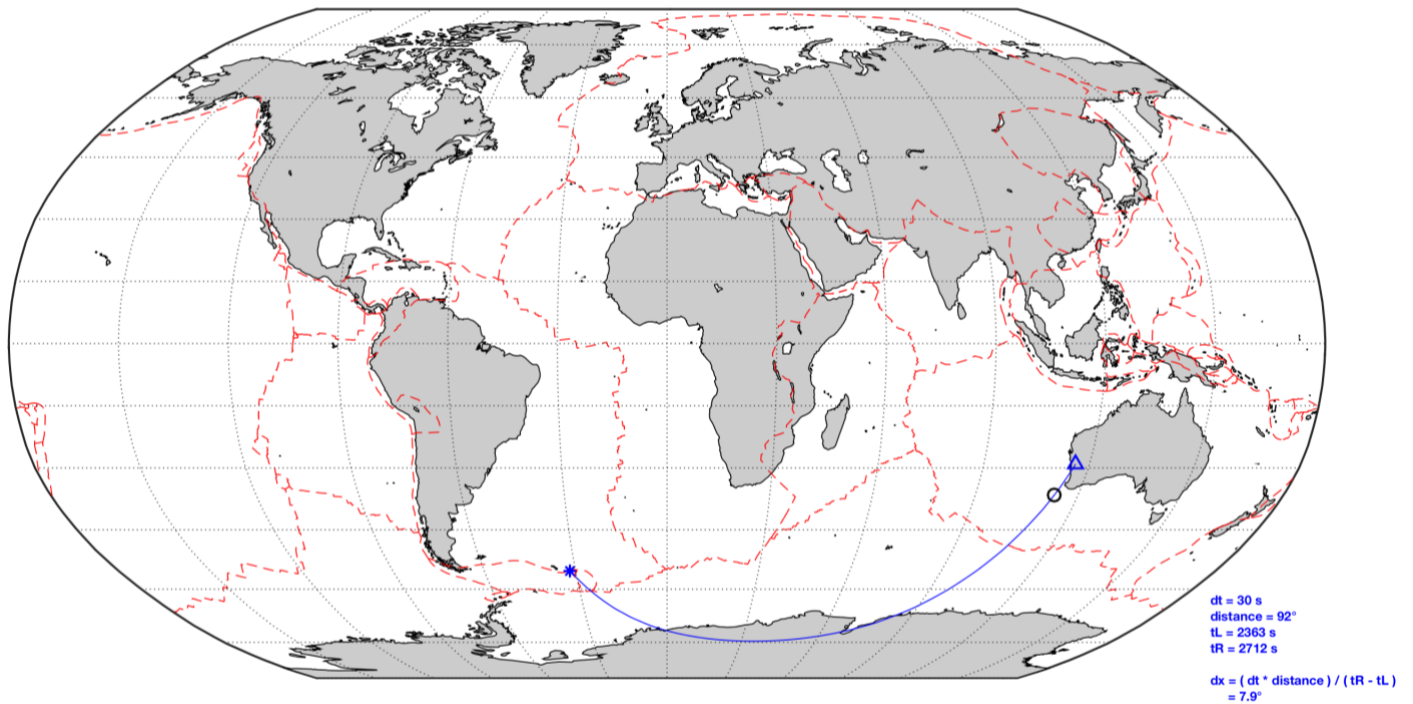


Figure S2. Map of QL wave example from Fig. S1. The location of the event (asterisk), seismic station MORW (triangle), and inferred QL scattering point (black circle) are plotted. The scatterer location is found by back-projecting a distance δx from the station along the raypath (blue line). In this example a QL delay time (δt) of 30 seconds was measured from the seismogram (Fig. S1) which equated to a distance of 7.9° for δx . Plate boundaries (dashed red line) are from ¹.

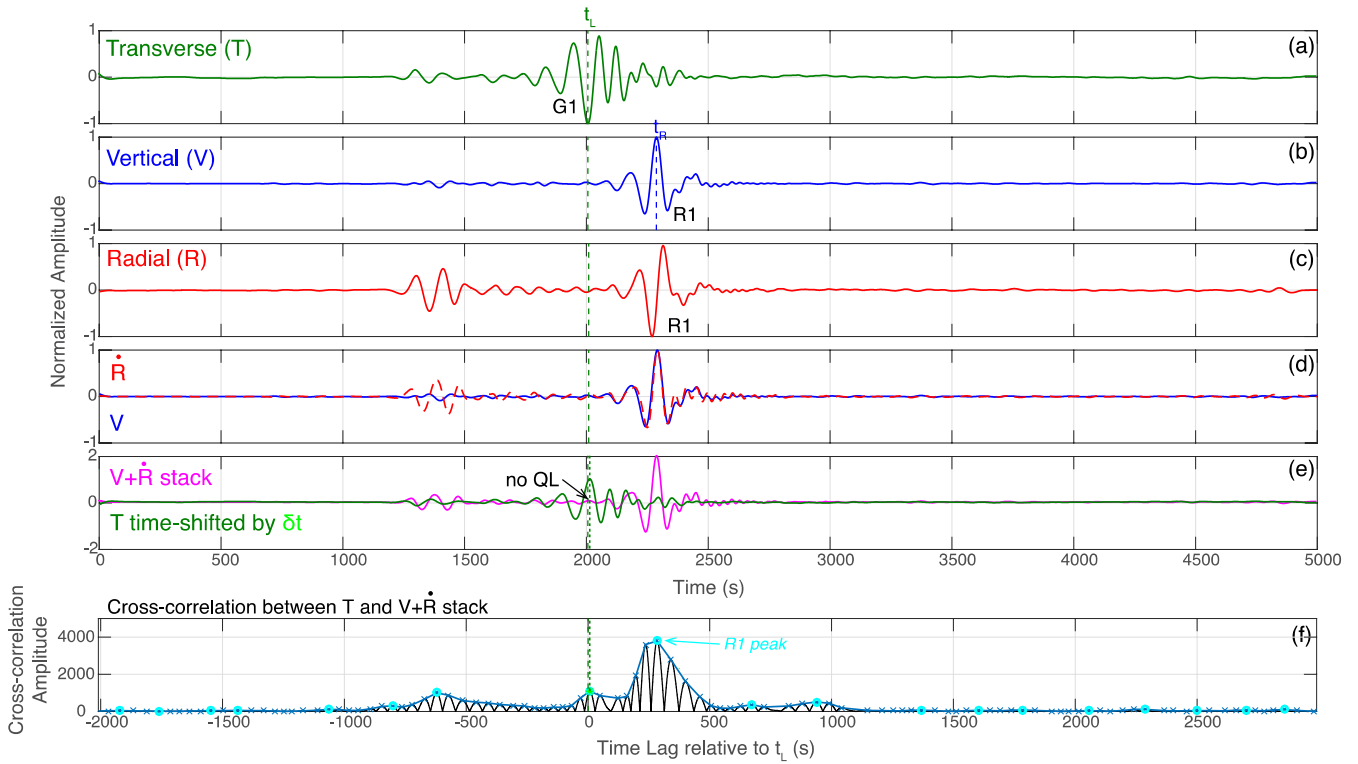


Figure S3. Example where no Quasi-Love (QL) wave was observed from station MTN near Darwin in the Northern Territory. The M6.7 event occurred on 05-Oct-2008 near the Tajikistan-Xinjiang Border. The SNR of this event is 12, and the epicentral distance is 74° , with a backazimuth of 318° . Plotting conventions are the same as for Fig. S1. In this example, both G1 and R1 are large amplitude arrivals but there is no distinguishable QL wave, resulting in a relatively flat cross-correlation function (f) between zero time-lag and the R1 peak.

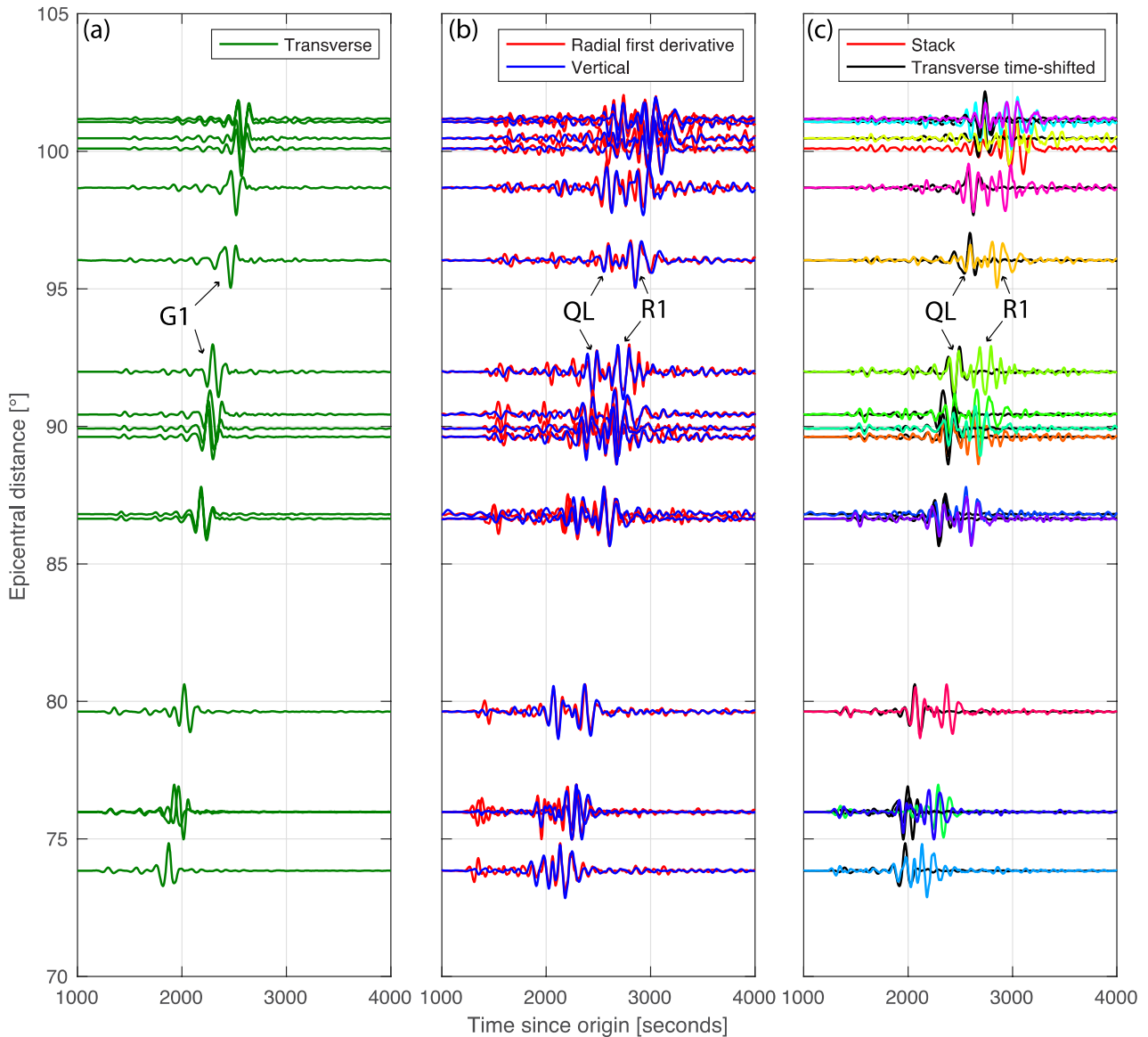


Figure S4. Seismograms showing detected QL wave arrivals from a single event, a M7.7 on 24th September 2013 in Pakistan (see Fig. S5). (a) The Love wave (G1) is prominent on the transverse component. (b) In all cases the QL wave arrival is seen clearly before the Rayleigh wave arrival (R1), visible on both the vertical (blue) and radial (red) components. Similar to R1, when the first derivative of the radial component is plotted, the QL wave motion is identical to that on the vertical component. These two components are summed together to produce the stack plotted in (c), and compared to the transverse component time-shifted by δt (black) to align the QL and G1 waves. The different colours of the stacked seismograms correspond to the recordings at various stations as shown in Fig. S5.

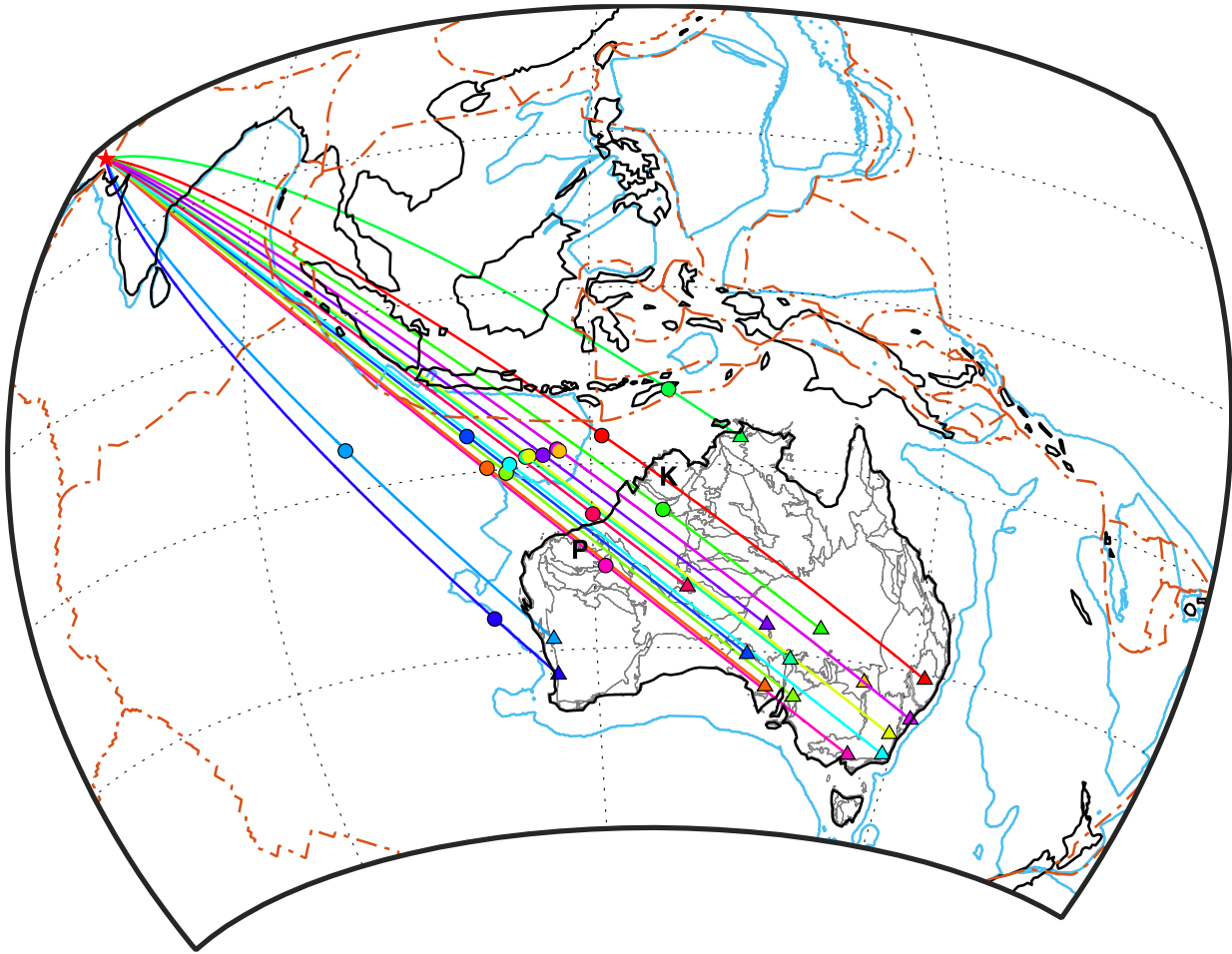


Figure S5. Map showing location and distribution of stations (coloured triangles) on which QL waves were detected for the M7.7 Pakistan event (red star) as shown in Fig. S4. The inferred location of the scatterer for each QL wave is shown by the solid-coloured circle along the great circle path. For this event, many stations suggest the presence of an anisotropic gradient to the northwest of Australia along the continental margin (light blue line). A couple of stations in southeast Australia detect QL scatterers associated with the edges of the Pilbara (P) and Kimberley (K) cratonic blocks in northwest Australia. Note that not all great-circle paths traverse the same geological structure within Australia (geological provinces outlined in grey). Where the geometry is favourable for Love-to-Rayleigh scattering in multiple locations along the path, the methodology employed here will only record the location of QL scattering that is closest to the seismic station. This may cause some variability in the detected scatterer locations.

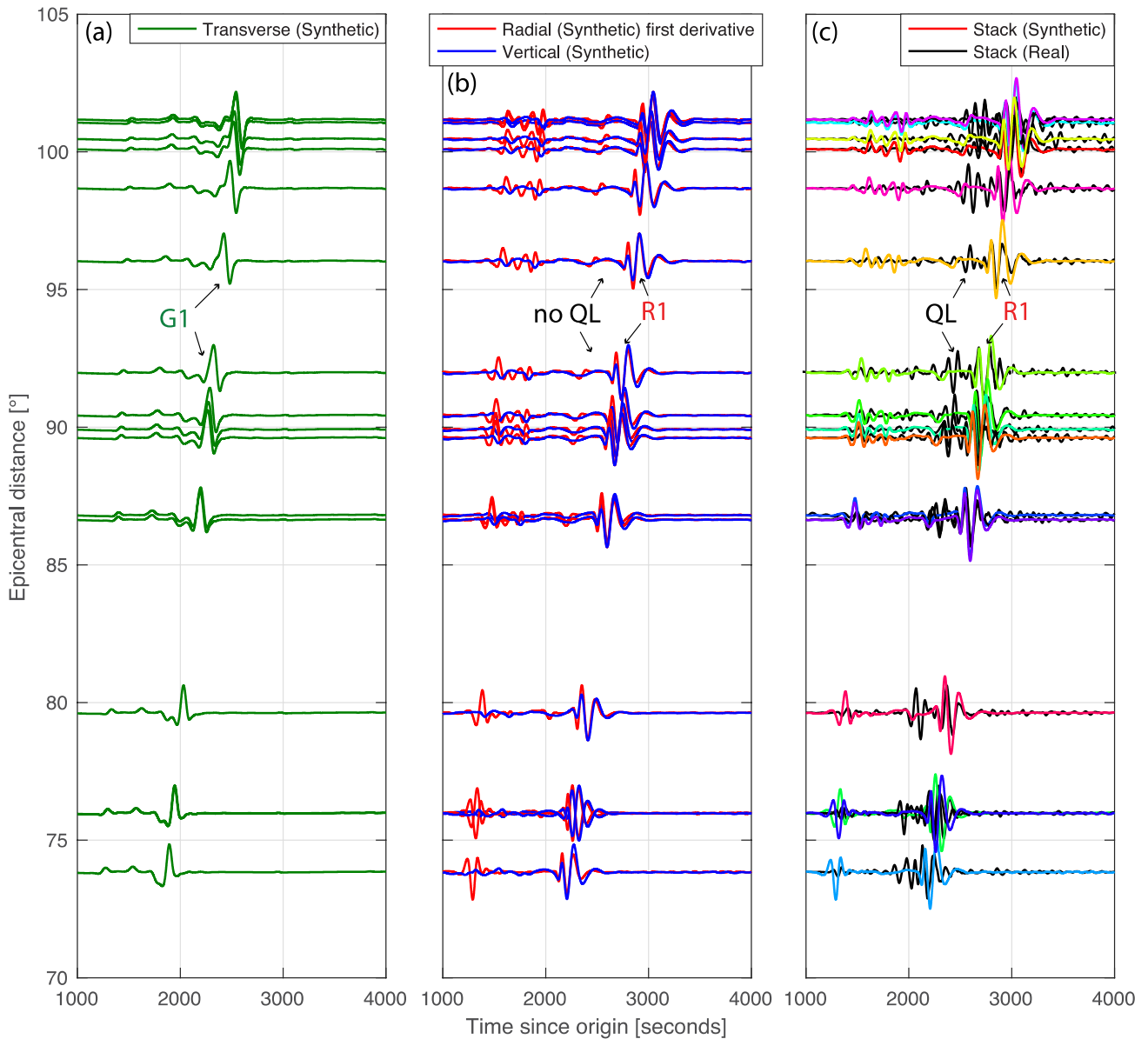


Figure S6. Same plots as Figure S4 except using synthetic seismograms for the 2013 M7.7 Pakistan event. Synthetic seismograms are generated for each source-receiver pair via the IRIS Synthetics Engine: Syngine²⁻⁵, using the source parameters from the Global Centroid Moment Tensor⁶ (event ID: C201309241129A) and the 1D PREM velocity model including radial anisotropy⁷. Synthetic seismograms are filtered and processed in the same way as for the real data. The fundamental Love (G1) and Rayleigh (R1) waves are prominent on the synthetic (a) transverse, and (b) vertical and radial components, as they are in the real data (Fig. S4). However, the Quasi-Love (QL) wave is noticeably absent on the synthetic vertical and radial components as the velocity model contains no lateral gradients in seismic anisotropy. When the vertical and first derivative radial components are stacked together to enhance elliptical Rayleigh wave motion (c), the R1 wave matches well between the synthetic (various colours) and real data (black) stacked seismograms, but the QL wave is only present on the real data, not the synthetics.

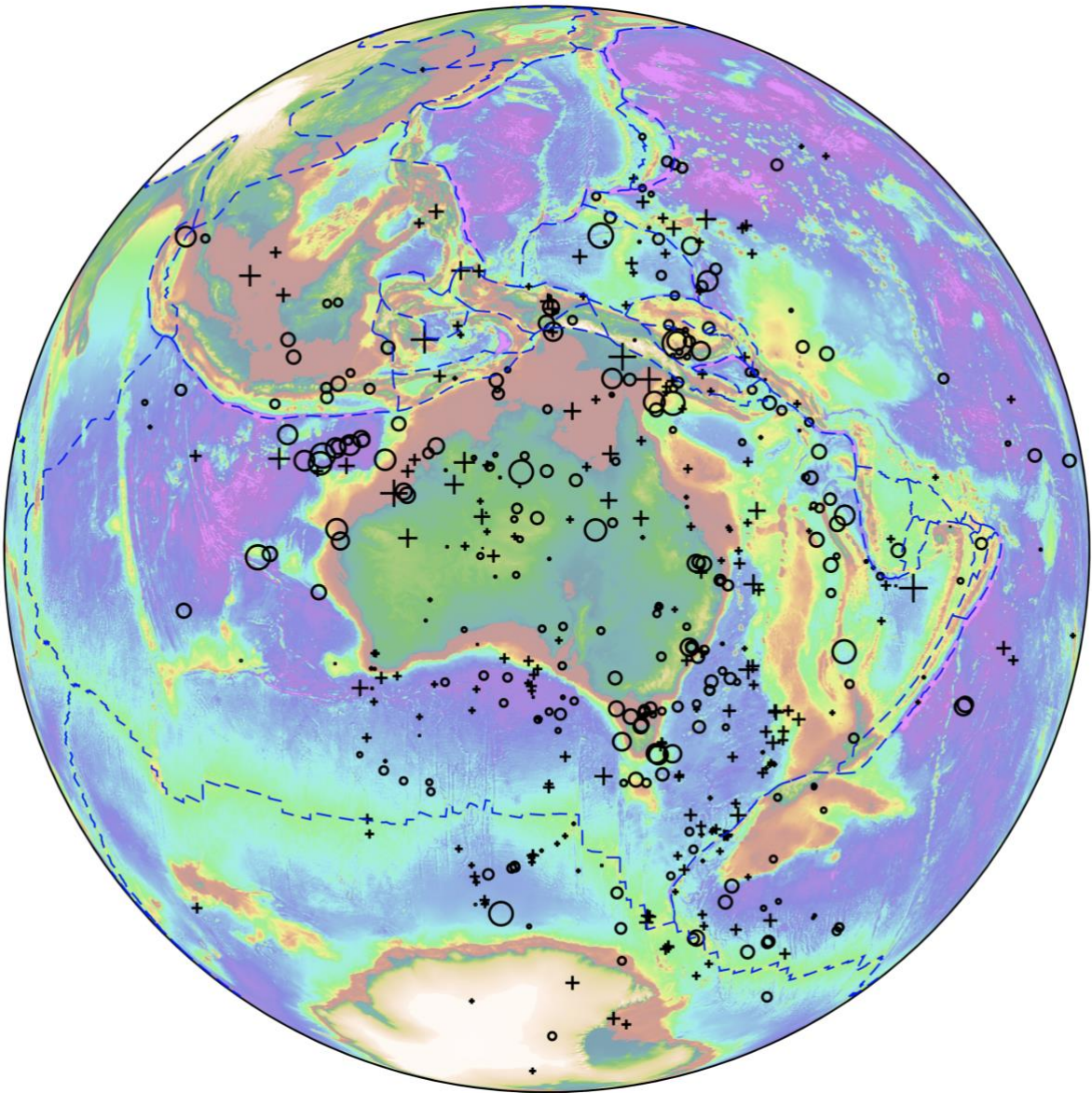


Figure S7. Map of all 498 QL wave scatterers found by this study. For the full listing of results see separate Supplementary Data Table S1. QL waves which displayed a positive correlation with G1 are represented by black crosses, and a negative correlation with black circles. Same as Figure 3, the size of the symbol is relative to the cross-correlation amplitude and the background colours show topography/bathymetry from ETOPO1 ⁸. Plate boundaries (dashed blue line) from ¹.

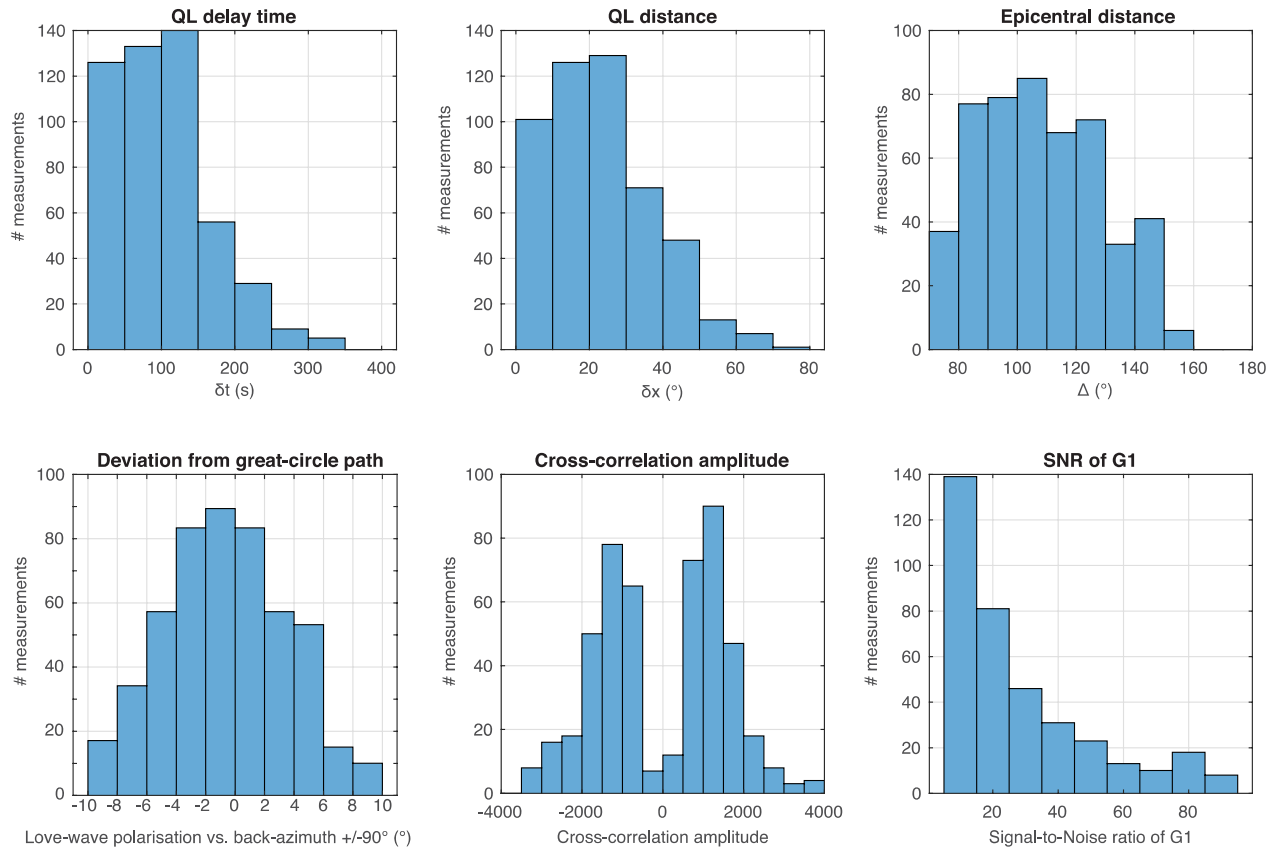


Figure S8. Histograms displaying properties of the QL measurements corresponding to the list of results in Table S1. The QL delay time, QL distance, and epicentral distance correspond to properties shown in Figure 1. The deviation from the great-circle path (lower left plot) is determined by measuring the polarisation angle of G1 in the horizontal plane (using the north and east components). The angular difference between the expected polarisation, which should be orthogonal to the source-receiver back-azimuth, and the observed polarisation, is then estimated. The cross-correlation amplitude (lower middle plot) is the value of the maximum cross-correlation between G1 and QL, i.e. the QL peak (green circle in Fig. S1f). It can be both positive and negative. The signal-to-noise ratio of G1 (lower right plot) is a comparison of the maximum amplitude of G1 to the amplitude of the noise in the first 300 seconds of the seismogram.

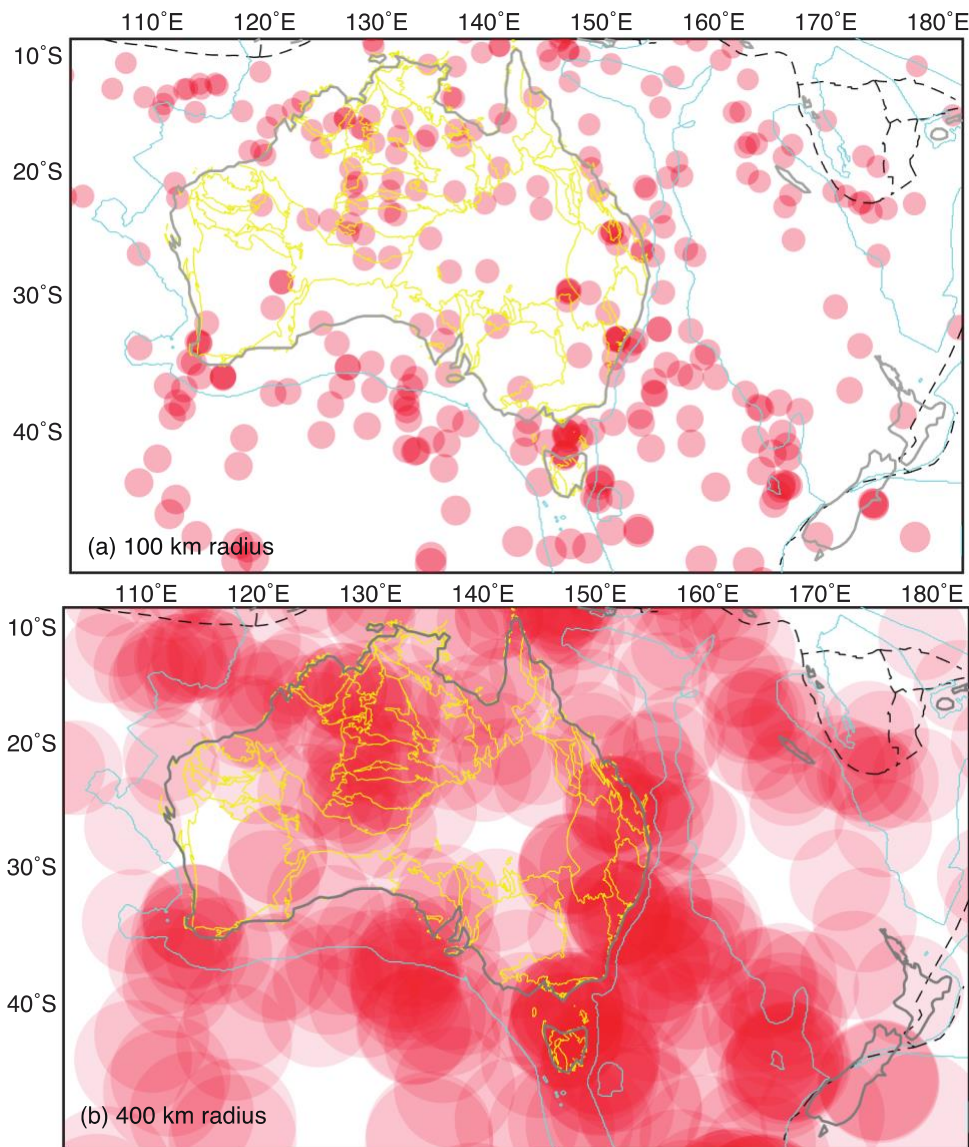


Figure S9. Map of QL scatterers (same as Fig. 3) with symbol size illustrating a location uncertainty of either 100 (a) or 400 (b) km radius. A location uncertainty of ~100 km is estimated to be typical, while ~400 km is considered likely to be the maximum (refer to description of uncertainties in Methods). Symbols are plotted semi-opaque to highlight density of measurements in certain areas. Even at 400 km radius, a higher density of results is visible along the southern margin of the Australian continent, on either side of the Tasman Sea, and within central to northern Australia.

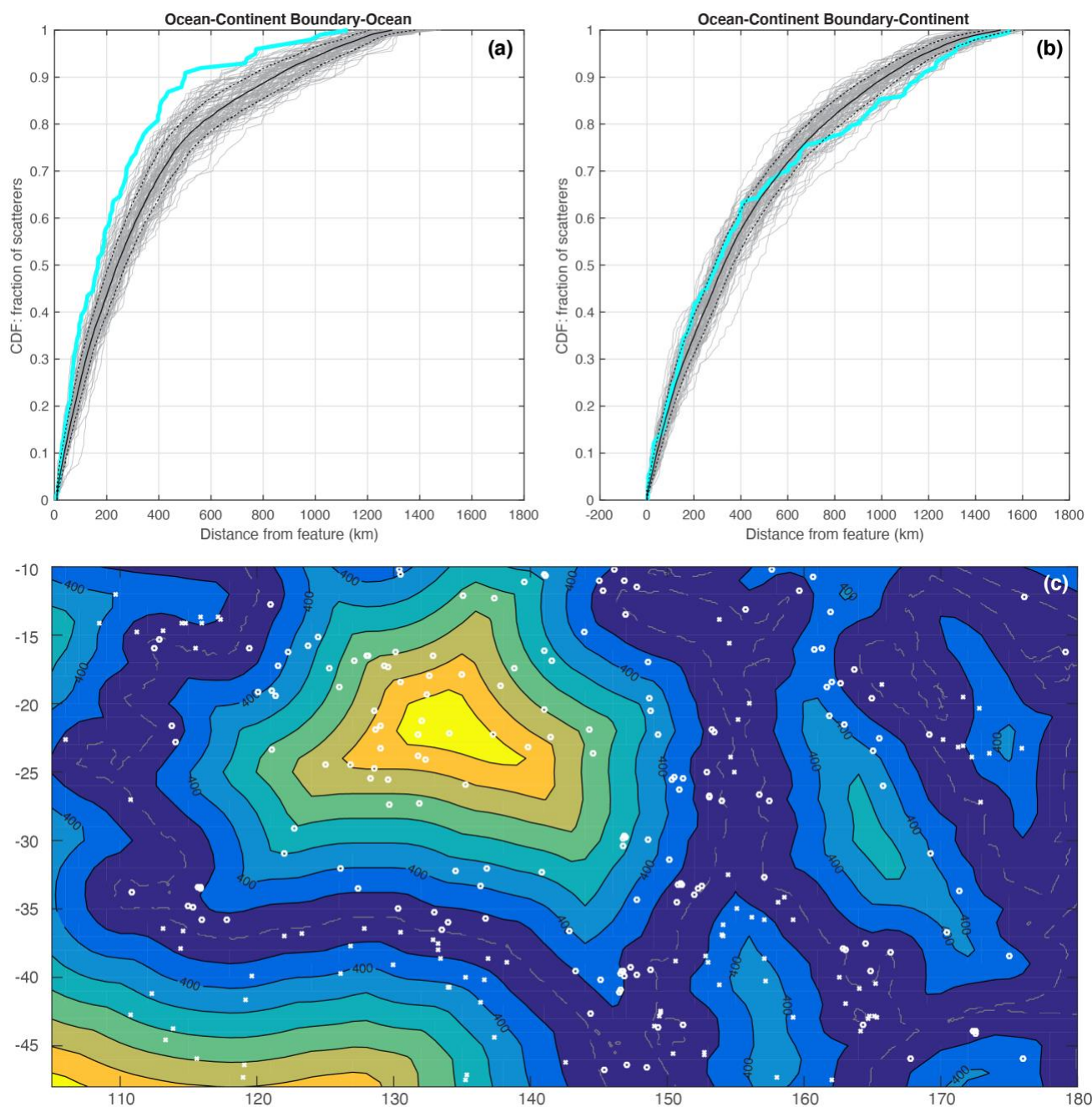


Figure S10. Cumulative distribution functions (CDF) showing the fraction of QL scatterers as a function of distance from the ocean-continent boundary (same as Fig. 4a), except separating the dataset into those that lie over the oceans (a) versus the continents (b). For the oceanic scatterers, a two-sample Kolmogorov–Smirnov test^{9–11} returns a p-value of 0.01, when comparing the CDF for these oceanic scatterers (cyan curve) with the mean (solid black curve) of 100 distributions of points randomly located across the oceans (thin grey lines). This indicates that the null hypothesis can be rejected at the 1% significance level. Across the study region oceanic crust covers 40% of the surface area, but accounts for 36% of the scatterers (99 out of 276 total). The CDF suggests that even though the number of scatterers in the oceans is slightly lower than expected than if they were uniformly distributed, they have a greater preference to be located closer to the continental margins. The same analysis, but for continental scatterers located on continental crust is shown in (b). The spatial correlation is less pronounced for the continental sub-set, with a greater similarity to the random distributions. The Kolmogorov–Smirnov test returns a p-value of 0.40, indicating that the null hypothesis cannot be rejected in this case. This may be due to the influence of internal geological

boundaries on QL scattering within the Australian continent (Fig. 4). In (c) a map showing zones of distance from the ocean-continent boundary (dashed grey line) is provided (same as Fig. 4c). Continental scatterers are plotted as small white circles, and oceanic scatterers as small white crosses.

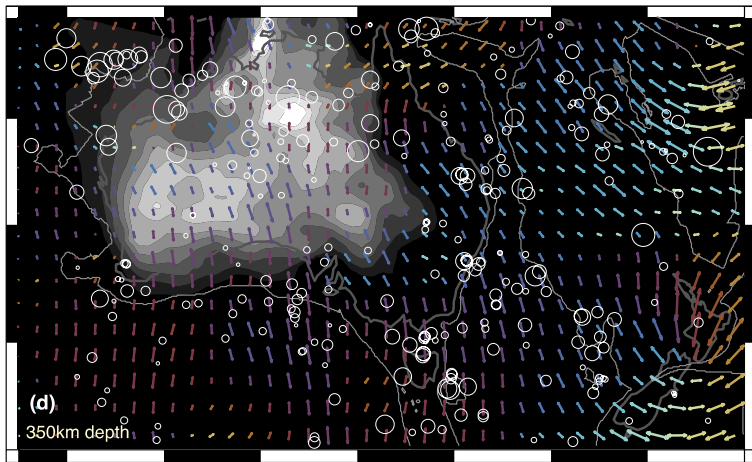
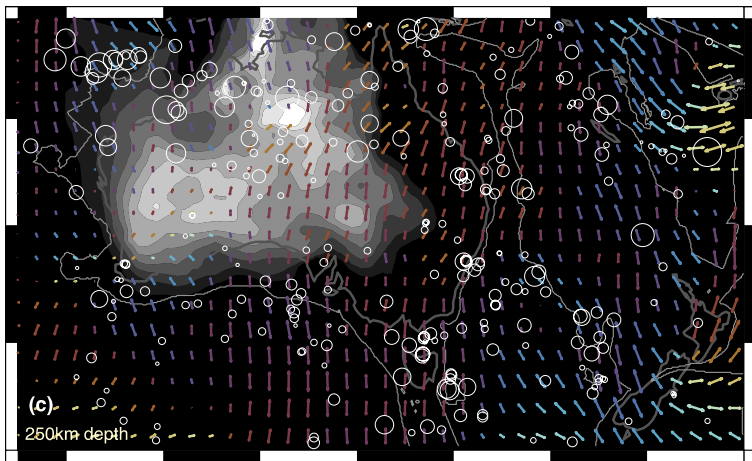
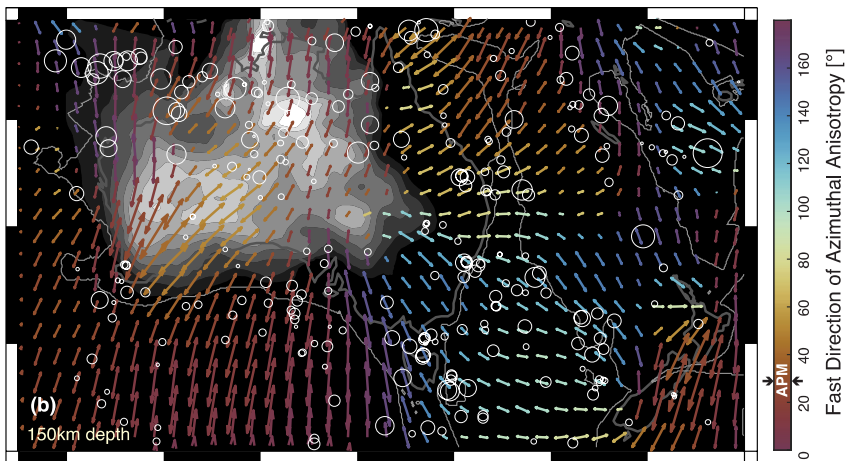
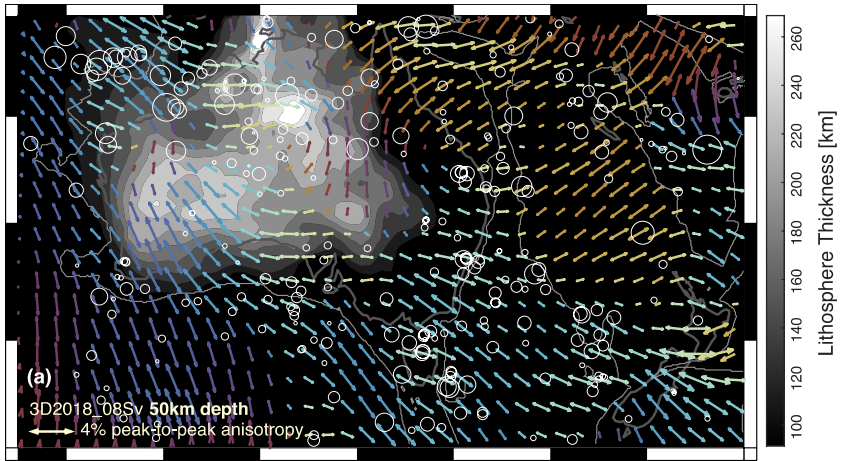


Figure S11. Azimuthal anisotropy derived from surface wave model 3D2018_08Sv¹² plotted at various upper mantle depths: (a) 50 km, (b) 150km, (c) 250 km, (d) 350 km. Plotting conventions same as Fig. 3d. Tomographic models, as shown here, present smoothed images of azimuthal anisotropy. While they cannot constrain lateral gradients in azimuthal anisotropy in the same way as QL scattering, together they provide complementary information about upper mantle anisotropic structure. The shallowest depth shown, 50 km, should be mostly sensitive to lithospheric anisotropy, showing considerable variation in the fast direction across the study area. There is a visible difference between the azimuthal anisotropy within Zealandia (yellow/orange colours) and that within the Tasman Sea (light blue colours), however the change is not reproduced on the other side of the Tasman Sea for the eastern Australian margin. At these shallow depths there is quite a bit of variation within the Australian continent too, suggestive of strong heterogeneity in fossil anisotropy, similar to that inferred by this study. As the depths become deeper the lateral variation in the azimuthal anisotropy model become less (i.e. more smooth or uniform). In the mid-asthenosphere (250 km) the fast directions are consistently N-S orientated across the study area (purple to mauve colours), indicating asthenospheric flow consistent with the absolute plate motion (APM).

References

1. Bird, P. An updated digital model of plate boundaries. *Geochemistry, Geophysics. Geosystems* **4**, (2003).
2. IRIS DMC. Data Services Products: Synthetics Engine. (2015). doi:<https://doi.org/10.17611/DP/SYNGINE.1>.
3. Nissen-Meyer, T. *et al.* AxiSEM: Broadband 3-D seismic wavefields in axisymmetric media. *Solid Earth* **5**, 425–445 (2014).
4. Van Driel, M., Krischer, L., Stähler, S. C., Hosseini, K. & Nissen-Meyer, T. Instaseis: Instant global seismograms based on a broadband waveform database. *Solid Earth* **6**, 701–717 (2015).
5. Krischer, L. *et al.* On-demand custom broadband synthetic seismograms. *Seismol. Res. Lett.* **88**, 1127–1140 (2017).
6. Ekström, G., Nettles, M. & Dziewoński, A. M. The global CMT project 2004–2010: Centroid-moment tensors for 13,017 earthquakes. *Phys. Earth Planet. Inter.* **200–201**, 1–9 (2012).
7. Dziewonski, A. M. & Anderson, D. L. Preliminary reference Earth model. *Phys. Earth Planet. Inter.* **25**, 297–356 (1981).
8. Amante, C. & Eakins, B. W. ETOPO1 1 arc-minute global relief model: procedures, data sources and analysis. *NOAA Tech. Memo. NESDIS NGDC-24* 19 (2009).
9. Kolmogorov, A. Sulla determinazione empirica di una legge di distribuzione. *G. della Ist. Ital. degli Attuari* **4**, 83–91 (1933).
10. Hoggard, M. J. *et al.* Global distribution of sediment-hosted metals controlled by craton edge stability. *Nat. Geosci.* **13**, 504–510 (2020).
11. Davies, D. R., Goes, S. & Sambridge, M. On the relationship between volcanic hotspot locations, the reconstructed eruption sites of large igneous provinces and deep mantle seismic structure. *Earth Planet. Sci. Lett.* **411**, 121–130 (2015).
12. Debayle, E., Dubuffet, F. & Durand, S. An automatically updated S -wave model of the upper mantle and the depth extent of azimuthal anisotropy. *Geophys. Res. Lett.* **43**, 674–682 (2016).